

# Collisional versus Collisionless Matter: a One-dimensional Analysis of Gravitational Clustering

Claudio Gheller<sup>1</sup>, Lauro Moscardini<sup>2</sup> and Ornella Pantano<sup>3</sup>

<sup>1</sup> Scuola Internazionale Superiore di Studi Avanzati, SISSA, via Beirut 2–4, I-34013 Trieste, Italy

<sup>2</sup> Dipartimento di Astronomia, Università di Padova, vicolo dell’Osservatorio 5, I-35122 Padova, Italy

<sup>3</sup> Dipartimento di Fisica Galileo Galilei, Università di Padova, via Marzolo 8, I-35131 Padova, Italy

arXiv:astro-ph/9501111v1 31 Jan 1995

6 June 2021

## ABSTRACT

We present the results of a series of one-dimensional N-body and hydrodynamical simulations which have been used for testing the different clustering properties of baryonic and dark matter in an expanding background. Initial Gaussian random density perturbations with a power-law spectrum  $P(k) \propto k^n$  are assumed. We analyse the distribution of density fluctuations and thermodynamical quantities for different spectral indices  $n$  and discuss the statistical properties of clustering in the corresponding simulations. At large scales the final distribution of the two components is very similar while at small scales the dark matter presents a lumpiness which is not found in the baryonic matter. The amplitude of density fluctuations in each component depends on the spectral index  $n$  and only for  $n = -1$  the amplitude of baryonic density fluctuations is larger than that in the dark component. This result is also confirmed by the behaviour of the bias factor, defined as the ratio between the r.m.s of baryonic and dark matter fluctuations at different scales: while for  $n = 1, 3$  it is always less than unity except at very large scales where it tends to one, for  $n = -1$  it is above 1.4 at all scales. All simulations show also that there is not an exact correspondence between the positions of largest peaks in dark and baryonic components, as confirmed by a cross-correlation analysis. The final temperatures depend on the initial spectral index: the highest values are obtained for  $n = -1$  and are in proximity of high density regions.

**Key words:** galaxies: clustering – galaxies: formation – large-scale structure of Universe

## 1 INTRODUCTION

In recent years a considerable improvement in the study of large-scale structure has been obtained with the development of three-dimensional codes able to follow simultaneously the evolution of dark and baryonic matter. It is important to include the gas in N-body simulations for at least two reasons: first we must estimate the large amount of gas that is observed in clusters of galaxies through X-ray emission; second, we must remove any ambiguity in the identification of galaxies. In the numerical simulations, the hydrodynamical equations have been solved either using mesh based methods (Chiang, Ryu & Vishniac 1989; Cen 1992; Ryu et al. 1993; Bryan et al. 1994) or particle methods like the smoothed particle hydrodynamics (Hernquist & Katz 1989; Evrard 1990; Katz & Gunn 1991). The latter, being Lagrangian methods, have the advantage of covering a larger range of clustering scales, but they are not very reliable in low density regions for the calculation of thermodynamical

quantities. Eulerian methods, on the contrary, give a better estimate of thermodynamical quantities, but are constrained by the limited grid resolution in their capability of following the collapse of high density regions. A large dynamical range can be attained only by increasing the number of grid-points, but this is obviously limited by the available computer memory. At present the largest mesh used in Eulerian calculations has  $256^3$  grid-points. The analysis of the evolution at different cosmological scales is obtained by changing the physical normalization of the box size, and sometimes the results obtained at a given scale are used for setting up initial and boundary conditions at another scale (e.g. Cen & Ostriker 1992).

Since three-dimensional calculations pose severe limits on the number of grid-points used in Eulerian methods, there has been in recent years an attempt to make up for the lack of resolution with the use of more accurate algorithms. One is looking for numerical methods able to well describe

both low density regions and strong gradients in the fluid flow. Very interesting is, for example, the possibility of introducing mesh refinement schemes in grid-based codes which, associated with shock capturing methods, would considerably improve the resolution in high density regions (Anninos, Norman & Clarke 1994).

The limited resolution reachable in three-dimensional codes makes sometimes difficult to separate, in the discussion of results, those effects which are only numerical from those which contains real physical information. Analysis like the one of Kang et al. (1994) are very useful for discriminating between different methods in three dimensions, but, because of the limitation in computer memory affecting all of the methods, a simultaneous one-dimensional analysis of the same phenomena appears quite convenient. Working only in a single dimension makes possible to span a large dynamical range and to follow structure formation at different scales. Approximate analytic solutions and their behaviour in highly non-linear regimes can also be better tested in one-dimensional calculations (e.g. Williams et al. 1991). Recently, Quilis, Ibáñez & Saez (1994) have studied the applicability of modern high-resolution shock-capturing methods to the study of cosmological structures in presence of pressure forces. However, they do not follow at the same time the dynamics of the dark matter and so they are not able to compare the clustering properties of the two different components. In our work, instead, we study the evolution of cosmological one-dimensional perturbations when both baryonic and dark matter are considered.

A detailed study of the evolution of gas and collisionless matter in a single pancake was presented by Bond et al. (1984) and Shapiro & Struck-Marcell (1985). In both of these works one-dimensional calculations of the coupled evolution of baryonic and dark component were performed including the effects of radiative and Compton cooling terms and thermal conductivity of the gas. The main difference between these two analyses is in the choice of the numerical algorithm used for solving the hydrodynamical equations which was Lagrangian in one case (Shapiro & Struck-Marcell 1985) and Eulerian in the other one (Bond et al. 1984). A similar analysis has been recently done by Thoul & Weinberg (1994), for a spherical configuration. They also have used a Lagrangian approach which has the advantage of giving a higher resolution where needed without having, in one-dimension, the same problems of grid distortion present in more dimensions. All of the previous one-dimensional works following the coupled evolution of dark and baryonic matter consider isolated perturbations in the expanding universe and start their simulations when hydrodynamical effects begin to become important in the evolution. The information concerning the formation epoch and mass of these isolated structures is derived from N-body calculations assuming some model of large-scale structure formation.

In this work we do not limit our attention to isolated perturbations but we want to explore the differences in the statistical properties of the one-dimensional clustering of baryonic and dark matter (hereafter BM and DM, respectively) components in an expanding background. We analyse the effect of pressure forces and adiabatic heating in the dynamics of the gas and we do not include, at this stage, cooling terms in our computations. Our aim is to understand first the evolution of one-dimensional structures only

in the presence of “compressible” effects. In addition, the inclusion of cooling processes requires the specification of characteristic time and length scales in the problem and in one-dimensional cosmological calculations it is not obvious how one can choose these quantities in connection with theory and observations. Therefore, we have preferred to make simulations which are scale-free; the absence of features in the primordial power-spectrum together with the higher spatial resolution implied by the use of one-dimensional simulations would permit to better discriminate between numerical artifacts and physical effects in the results. At the end, physical information on the computed quantities can easily be extracted by fixing the normalization quantities, like the box size and the final time.

The plan of the paper is as follows. In Section 2 we introduce the dynamical equations both for the hydrodynamical variables and for collisionless matter. The numerical methods used for the solution of these equations are also presented together with some numerical tests. The results obtained in numerical simulations of cosmological one-dimensional structures are shown in Section 3. Discussion and conclusions are drawn in Section 4.

## 2 DYNAMICAL EQUATIONS

In this section we present the dynamical equations that we use for evolving the BM and DM components in the case of one-dimensional perturbations. We assume a flat universe ( $\Omega = 1$ ) in which the BM component accounts for 10% of the total mass ( $\Omega_{BM} = 0.1$ ) and the rest is in the form of DM ( $\Omega_{DM} = 0.9$ ). In the present analysis we neglect the effects of radiative and Compton coolings and any possible external heating. The DM component is approximated as a pressureless fluid and the BM component as a perfect fluid.

### 2.1 Hydrodynamical equations

We introduce the following set of dimensionless variables:

$$\tilde{t} = \frac{t}{t_0}, \quad (1)$$

$$\tilde{x} = \frac{x}{x_0}, \quad (2)$$

$$\tilde{v} = v \frac{t_0}{x_0}, \quad (3)$$

$$\tilde{\varrho} = \frac{a^3 \varrho}{\varrho_0}, \quad (4)$$

$$\tilde{\epsilon} = a^3 \epsilon \frac{t_0^2}{\varrho_0 x_0^2}, \quad (5)$$

$$\tilde{\phi} = \phi \frac{t_0^2}{x_0^2}, \quad (6)$$

where  $x$  is the comoving coordinate,  $t$  is the time,  $a = \tilde{t}^{2/3}$  is the cosmological expansion factor,  $\phi$  is the peculiar gravitational potential,  $\varrho$  and  $\epsilon$  are the matter and internal energy densities, respectively. We have three basic units of normalization: the final time  $t_0$ , the comoving cell size  $x_0$  and the mean baryon density  $\varrho_0$  at time  $t_0$ . For a cosmological application we can take  $t_0$  and  $\varrho_0$  equal to the present age and density of the Universe, respectively.

The evolution of the collisional component is described by the following set of hydrodynamical equations:

$$\frac{\partial \tilde{\varrho}}{\partial \tilde{t}} + \frac{1}{a} \frac{\partial}{\partial \tilde{x}} [\tilde{\varrho} \tilde{v}] = 0, \quad (7)$$

$$\frac{\partial \tilde{\varrho} \tilde{v}}{\partial \tilde{t}} + \frac{1}{a} \frac{\partial}{\partial \tilde{x}} [\tilde{\varrho} \tilde{v}^2 + \tilde{p}] = -\frac{\dot{a}}{a} \tilde{\varrho} \tilde{v} - \frac{1}{a} \tilde{\varrho} \frac{\partial \tilde{\phi}}{\partial \tilde{x}}, \quad (8)$$

$$\frac{\partial \tilde{\epsilon}}{\partial \tilde{t}} + \frac{1}{a} \frac{\partial}{\partial \tilde{x}} [\tilde{\epsilon} \tilde{v}] = -2 \frac{\dot{a}}{a} \tilde{\epsilon} - \frac{1}{a} \tilde{p} \frac{\partial \tilde{v}}{\partial \tilde{x}}, \quad (9)$$

where  $\tilde{p}$  is the comoving pressure.

We use the equation of state of an ideal gas with adiabatic index  $\gamma = 5/3$ , so that

$$\tilde{p} = (\gamma - 1) \tilde{\epsilon}. \quad (10)$$

The physical temperature  $T$  is related to the previous normalized quantities by

$$T = 2 \frac{m_p}{K_B} \frac{(x_0)^2 \tilde{\epsilon}}{t_0} \frac{1}{\tilde{\rho}}, \quad (11)$$

where  $K_B$  is Boltzman's constant and  $m_p$  the mass of the proton.

## 2.2 Collisionless matter

In the dynamical equations for the collisionless particles we use as time integration variable the scale factor  $a$ :

$$\frac{d\tilde{x}}{da} = \tilde{u}, \quad (12)$$

$$\frac{d\tilde{u}}{da} + \frac{3}{2a} \tilde{u} = -\frac{9}{4a} \frac{\partial \tilde{\phi}}{\partial \tilde{x}}. \quad (13)$$

The peculiar gravitational potential due to both the BM and DM component is computed by solving the Poisson equation:

$$\frac{\partial^2 \tilde{\phi}}{\partial \tilde{x}^2} = \frac{K}{a} (\tilde{\varrho}_{BM} + \tilde{\varrho}_{DM} - 1), \quad (14)$$

where  $K = 4\pi G \varrho_0 t_0^2$  and  $G$  is the Newton's constant.

## 2.3 Numerical Methods

The hydrodynamical equations have been integrated using the Flux Corrected Transport (FCT) method (Boris & Book 1973; Zalesak 1979), a hybrid shock capturing method. In this method two difference schemes are blended together: a second order Lax-Wendroff scheme is used in regions of smooth flow, while a first order Lax scheme is used near discontinuities. Then second order accuracy is ensured everywhere except near flow jumps where the dissipation introduced by the low order scheme guarantees monotonicity in the behaviour of flow variables. The blending between the two schemes is controlled by a monotonicity constraint that leads to the sharpest possible discontinuity profiles. However, if the grid is not sufficiently fine, very strong gradients can be represented as a sequence of discontinuous jumps. This effect usually does not hinder the convergence of the method and can be reduced or completely avoided refining the grid (Woodward & Colella 1984).

For the integration of the collisionless matter we have used a particle-mesh code (Hockney & Eastwood 1981). We use the same mesh as in the hydrodynamical part of the

code, while the number of particles is a multiple of the number of mesh points in order to have a good resolution also in low density regions. The interpolation used for computing the mass density and the forces acting on each particle is obtained by a TSC scheme (e.g. Hockney & Eastwood 1981), which ensures a good accuracy in the estimates of previous quantities without leading to an excessive slowing down of the computation. For the time integration we use a second order leap-frog method so that the accuracy in the N-body is comparable to that attained in the hydrodynamical part of the code. The peculiar gravitational potential is computed using the standard fast Fourier transform technique.

The accuracy of the code has been tested against known analytical solutions. For the hydrodynamical part we performed the shock tube test comparing the analytical and numerical solutions. We found a very good agreement in smooth regions, while the shock is numerically diffused over about five grid-points. The evolution of an initial sinusoidal perturbation has been instead used for testing the performance of the N-body code: in this case the numerical solution has been compared with the results obtained using the Zel'dovich approximation (Zel'dovich 1970) which provides the exact one-dimensional solution up to shell crossing. In Figure 1 we compare, just before shell crossing, the resulting DM distributions for the Zel'dovich and N-body solutions for two different choices of the number of grid-points  $N_g$  ( $N_g = 2^{10}$  and  $N_g = 2^{15}$ ). The number of particles is instead kept fixed and set equal to  $2^{16}$ . We notice that already with the smallest number of grid-points the N-body solution is in very good agreement with the Zel'dovich result. The difference in the height of the peak in the two cases is only due to the different numerical resolution implied by the adopted grids.

We used a sinusoidal perturbation also for testing the coupled evolution of dark and baryonic components and to see how far the code is able to follow the collapse of a baryonic fluctuation. In Figure 2 we show the density profile of both components after the shell crossing time, obtained using a grid of  $2^{15}$  points. We can see that fluctuations in the baryonic matter as larger as  $10^2$  can be easily resolved with this resolution. Some typical problems of the FCT method start to appear after the formation of strong shocks which are not well resolved using the previous grid, but they do not destroy the solution and a local spatial refinement would permit to continue the evolution. Since situations as this one are never found in the following cosmological simulations, we believe that a grid of  $2^{15}$  is sufficient for our purposes.

## 3 COSMOLOGICAL ONE-DIMENSIONAL STRUCTURES

In this section we present the results of the evolution of one-dimensional perturbations in an expanding background. We analyse the distribution of BM and DM, paying particular attention to the clustering properties of the two components and to the effects due to their coupling.

### 3.1 Numerical Simulations

We consider a grid of comoving length  $L$ , whose physical size grows according to the expansion parameter  $a$ . We sub-

divide our grid into  $2^{15}$  nodes and adopt periodic boundary conditions. The number of particles used in the N-body part of the code is  $2^{16}$ .

The initial conditions for a given model are determined as follows. The DM component is perturbed according to a Gaussian random density field characterized by a power-law spectrum of the general form

$$P(k) = Ak^n \exp(-k^2 R_f^2), \quad (15)$$

where  $A$  is a normalization constant and  $n$  the spectral index. The short wavelength cut-off at the scale  $R_f = 2$  grid-points ensures that the results are not affected by the sampling of modes whose size is close to that of the resolution of the simulation.

The normalization constant  $A$  is fixed requiring that the one-dimensional variance  $\sigma^2$  at the final time  $t_0$  (corresponding to the expansion factor  $a = 1$ ) for linearly evolved perturbations is equal to unity. In computing the variance we assume a filtering radius  $R_\star = 10^{-2}L$  so that

$$\sigma^2(R_\star) = \frac{1}{\pi} \int_0^\infty P(k) W^2(k, R_\star) dk. \quad (16)$$

The function  $W(k, R_\star)$  is a one-dimensional top-hat filter:

$$W(k, R_\star) = \frac{\sin(kR_\star)}{kR_\star}. \quad (17)$$

Initially the DM particles are evolved according to the Zel'dovich (1970) algorithm which is known to give the exact solution up to the shell crossing. We start our numerical computation when one of the following requirements is satisfied: i) the largest density fluctuation is equal to unity; ii) the first shell crossing has occurred: this typically corresponds to epochs with  $a < 10^{-3}$  for all models.

The numerical evolution of BM starts when  $a = 10^{-3}$ , i.e. just after the recombination epoch. Before this time we assume that the distribution of BM is constant, as it would be in comparison with DM distribution, because of the coupling between radiation and baryonic matter before hydrogen recombination. The internal energy is fixed assuming that the cooling of the gas is due only to adiabatic expansion between the epoch of recombination and the initial time of the simulations. In the subsequent evolution the perturbation in the baryonic matter is induced by gravitational coupling with the DM component.

As already pointed out, our simulations are completely scale-free: the final amplitude of the fluctuations depend only on the scale  $R_\star$  relative to which the initial normalization is fixed. The final thermodynamical quantities are completely determined once the amplitude of initial perturbations and the initial value of  $\tilde{\epsilon}$  are given. For example, if we think of  $R_\star$  as corresponding of  $8 h^{-1}$  ( $h$  is the Hubble constant in units of  $100 \text{ km s}^{-1} \text{ Mpc}^{-1}$ ), where observationally the variance is found to be unity, the whole box would correspond to  $L = 800 h^{-1} \text{ Mpc}$  (we use  $R_\star = L/100$ ) and then we would be looking the evolution at very large scales. In order to study the evolution on smaller scales but fixing the normalization of the initial spectrum at the same physical scale, we should use a larger value for  $R_\star$  in units of  $L$  and, consequently, we should start with larger density fluctuations. These simulations would produce larger final temperatures on these smaller scales as we expect.

### 3.2 Results

We consider three different models with primordial spectral index  $n = -1, 1, 3$ : in three dimensions, these would correspond to  $n = -3, -1, 1$  (the so-called Harrison-Zel'dovich spectrum) respectively, covering in this way the range of values usually adopted for cosmological models. For each model we run three simulations with different realizations of the initial conditions in order to obtain more accurate estimates of the relevant quantities. Here we consider various statistical tests, such as the distribution of density perturbations, peaks and thermodynamical quantities, their correlations and the density power-spectrum. The results referring to the DM component have been previously smoothed by a Gaussian filter with a radius of ten grid-points, roughly corresponding to twice the numerical spreading of the shock front in the hydrodynamical calculations.

#### 3.2.1 Distribution of Density Perturbations

In Figures 3a and 3b we show the behaviour of  $\delta_{BM}$  and  $\delta_{DM}$  in a realization for each model at two different epochs:  $a = 0.5$  and the final one  $a = 1$ , respectively. The results refer to about a tenth of the whole grid. Different runs of the same model show a very similar qualitative behaviour. The density fluctuations are computed with respect to the mean value of the corresponding component. As expected, increasing the spectral index  $n$ , we have less power on large scales and, consequently, peaks in density contrast are more frequent, but they have a smaller density contrast, while underdense regions are less extended. We notice that only for  $n = -1$  peaks in BM are higher than those in DM and their contribution to the local gravitational field starts to be comparable to that of DM.

For the  $n = 3$  case there is a correspondence between the distribution of DM and BM although there are always substructures in the collisionless component which are not present in the other one (see also the following discussion on relative bias, power-spectrum and number of peaks). This behaviour is enhanced as we decrease the spectral index: BM appears more and more clumped while DM stays more spread with small substructures. This is particularly evident in the structures appearing in the model with  $n = -1$ , where collisionless matter is spread over a region which is several times larger than that occupied by the peak in BM. It is interesting to notice also that there is not an exact correspondence between the positions of the largest BM and DM peaks.

Comparing the figures at two different times we see the tendency to the merging of substructures which produces higher peaks and larger voids. This behaviour is again more evident in simulations with more power on large scales. For example, in the panels referring to the  $n = -1$  simulation, it is possible to note that the two central peaks in the BM component at  $a = 0.5$  quickly merge forming a unique high-density region at  $a = 1$ . This phenomenon is less pronounced for DM, which at  $a = 1$  continues to be divided into small substructures.

A quantitative estimate of the spatial correspondence between the BM and DM density distributions can be obtained studying the cross-correlation coefficient (see e.g. Coles, Melott & Shandarin 1993)

$$S(R) = \frac{\langle \delta_{BM}(R) \delta_{DM}(R) \rangle}{\sigma_{BM}(R) \sigma_{DM}(R)}, \quad (18)$$

where  $\delta_{BM}$  and  $\delta_{DM}$  are respectively the density contrasts in the BM and DM components, smoothed with a Gaussian window of radius  $R$  and  $\sigma_i = \langle \delta_i^2 \rangle^{1/2}$  are the corresponding r.m.s.. The mean is computed over all grid-points. Definition (18) implies  $|S| \leq 1$ . The limit  $S = +1$  corresponds to  $\delta_{BM} = C\delta_{DM}$ , where  $C$  is a constant: in this case there is a perfect agreement in the positions of the structures in the two components. In Figure 4, the cross-correlation coefficient  $S$  is plotted as a function of the Gaussian filtering radius  $R$  for the three models when  $a = 0.5$  and  $a = 1$ . The error bars, shown for clarity only at the final time, represent the scatter r.m.s. between the three different realizations of each model. At earlier times these errors are found to be always smaller. As expected, decreasing the filtering radius and/or allowing for a longer evolution, the differences between the two components increase and, consequently, the coefficient  $S$  decreases. This is particularly true for the model with  $n = -1$ , where, for small  $R$  (up to  $L/400$ ), the cross-correlation is even less than 0.4, denoting the small correspondence between BM and DM distributions which was already clear in Figure 3. On the contrary, a value of  $S$  close to unity is obtained in the simulations with  $n = 3$ , even when a small filtering radius is adopted.

The study of high-density regions in BM is particularly interesting because they are expected to be related to the positions where galaxy formation occurs. We define as peaks all the grid-points which are local maxima of the density fluctuation field. In Figure 5 we show, at two different times, the number of peaks  $N_{pk}$  having an height greater than a given threshold  $\delta$ , both for BM and DM components. The comparison between the models with different spectral indices shows once again a different behaviour. Only for the model with  $n = -1$ , the number of high peaks in BM is larger than that of DM at both considered times. The latter model is also the one which shows the largest time evolution in the number of peaks. In the other cases,  $N_{pk}$  does not change significantly and the peak number in the BM component is always less than that in DM one.

### 3.2.2 Thermodynamical quantities

In Figure 6 we show the behaviour of the baryonic quantities  $\tilde{\varrho}_{BM}$ ,  $\tilde{p}$  and  $T$  for the case  $n = -1$  at  $a = 1$  (the results refer to the same realization shown in the upper panel of Figure 3b but in this case the whole grid is displayed). This is the model in which the highest values in thermodynamical quantities are obtained, thus some effects, which are also present in the other models, are better visible. The baryonic density and the pressure are given in normalized units, while the temperature is shown in Kelvin degrees. In absence of heating from external sources and cooling processes, we notice a strong correspondence among peaks in density, pressure and temperature. However, in correspondence of the largest density fluctuations we observe a double peak on the top of the temperature profile which shows, as expected, that heating mainly occurs in the regions in which the velocity gradient is large.

The temperature distribution in the different models is better illustrated by the cumulative volume filling factor

and mass fraction  $F$  as a function of the temperature  $T$ . Figure 7 shows the behaviour of these quantities at  $a = 1$  as obtained by summing over the contribution of all three realizations for each model. We notice that the fraction of matter at high temperature (e.g.  $T \geq 10^4$  K) increases as we decrease the spectral index: it is approximately 15% and 2% for  $n = -1$  and  $n = 1$ , respectively, while no grid-point has such a high temperature in the  $n = 3$  model (in this case the highest temperature obtained is about 25 K). At the same time, most of the volume is at low temperatures: this is particularly evident in the case  $n = -1$ , where, due to the dominance of empty regions, more than 90% of the volume has  $T \leq 10^{-1}$  K. On the contrary, the two cumulative functions are more similar in the model with  $n = 3$ , where structures are smaller and more uniformly distributed. These results suggest that, in absence of other dissipative or heating effects (viscosity, thermoconduction, starbursts, etc.), it is difficult to obtain from one-dimensional cosmological large-scale perturbations temperatures as high as those seen in X-ray observations.

Figure 8 shows contour plots for the number of zones characterized by a given temperature and baryonic density. The additional information which we can extract from these graphs is the correlation between these two quantities in all the three models. This correlation is particularly strong in the case  $n = -1$  and refers to the large empty regions characterizing this model. On the contrary, more scattered distributions are presented in the models with  $n = 1$  and  $n = 3$ .

### 3.2.3 Power-spectrum and bias

In order to study the time evolution of clustering at different scales, we have computed the power-spectrum  $P(k)$ . If the density fluctuations remain linear at large scales,  $P(k)$  is expected to grow as  $a^2$ . In Figure 9 we show the behaviour of the power-spectrum both for DM and BM for the three models at different times. The units of the wavenumbers  $k$  are such that  $k = 1$  corresponds to the fundamental wavelength of the computational grid. Considering the models with  $n = 3$  and  $n = 1$ , we see that at small wavenumbers (i.e. at large scales) the growth of the perturbations in the DM component is in good agreement with linear theory. The situation is different for the model with  $n = -1$  where the growth of perturbations is non-linear even at these scales. At larger wavenumbers (i.e. at small scales) deviations from linear theory are found, as expected. In particular, we notice that there is a faster evolution for the models with  $n = -1$  and  $n = 1$ : the non-linear growth produces the coupling of high- and low- $k$  modes. In the model with  $n = 3$ , where initially the large-scale power is small, this effect does not appear. Then, our simulations, even if starting with a power-law spectrum, seems to exclude the possibility of having self-similar evolution when large scale power is present. Only the model with  $n = 3$  presents a self-similar evolution in the DM at least for  $\log k \leq 2.4$ .

The behaviour of the BM is very different. At the beginning, due to the assumption of uniform distribution on all scales, the power-spectrum is zero. At early times all models show a very slow growth produced by the coupling with the DM fluctuations (the curves for the model  $n = -1$  are not visible because  $P(k)$  is too low). Only at late epochs

( $a \approx 0.5$ ), the fluctuations in the BM grow considerably and quickly reach those in the DM. At the final time  $a = 1$  the power-spectra in the two components are different at small scales, where the growth of gas perturbations is delayed by the pressure: this is particularly true in the models with  $n = -1$  and  $n = 1$ , for which higher values of the pressure are reached.

An interesting way to measure the relative growth of the perturbations is the bias factor  $b$ , defined as

$$b(R) = \frac{\sigma_{BM}(R)}{\sigma_{DM}(R)}, \quad (19)$$

where  $\sigma_i^2(R)$  is the variance of the density fluctuation field in the  $i$ -component, smoothed using a Gaussian window of radius  $R$ . Figure 10 shows the behaviour of  $b$  for the three models at  $a = 0.5$  and  $a = 1$ . The scatter r.m.s. between the different realizations of each model is also plotted only at the final time. The models with  $n = 1$  and  $n = 3$  behave in a similar way: the DM appears more clustered than the BM at small scales, while at larger scales they tend to have the same clustering properties. As expected, the pressure in the BM prevents shell-crossing and a collapse comparable to that occurred in the DM. At larger scales where dissipation is negligible, the two distributions are similar. In the case  $n = -1$  instead, the BM at the final time  $a = 1$  has a larger variance than the DM component at all scales; this is in agreement with the density distribution shown in Figure 3b. The motivation for the different behaviour of this model is the large peculiar velocities of the DM component. In fact, the absence of dissipative effects delays the formation of more compact structures. In the BM, instead, higher temperatures and pressures are reached, but they are not sufficient to overcome the gravitational force and avoid the collapse. In addition the conversion of the kinetic into internal energy allows the formation of more compact baryonic structures.

From Figure 10 it is possible to extract also information about the time evolution of the bias factor. Again we can note a different behaviour between the models. In the case  $n = -1$ , the evolution of  $b$  from  $a = 0.5$  to  $a = 1$  is rapid at all scales:  $b$  changes by a factor  $\approx 1.5$ . On the contrary, the increase of  $b$  in the same time interval is smaller for  $n = 1$  and  $n = 3$  (approximately 15% and 5%, respectively) but the final value is always below unity.

#### 4 DISCUSSION AND CONCLUSIONS

In this paper we have studied the evolution of one-dimensional perturbations in a medium composed by BM and DM. Initial Gaussian perturbations with a power-law spectrum are assumed in the dominant DM component and then the perturbations in the BM component, initially uniformly distributed, are induced through gravitational coupling. We observe that BM does not fall immediately into the potential wells created by the distribution of the collisionless component, but when this happens, the amplitude of density perturbations in the gas becomes quickly comparable to that of the DM. At large scales the final distribution of the two components, as shown by the cross-correlation coefficient and by the bias factor, is very similar. The main differences are present at small scales where the DM compo-

ment presents a lumpiness which is not found in the BM. A quite important feature shown by all simulations is the non-exact correspondence between largest DM and BM peaks.

In our simulations peaks in the DM are always higher than those in BM except for  $n = -1$ , i.e. for the spectrum with more power on large scales. In this case the variance in baryon density distribution is larger than that of DM at all scales. Moreover, in the highest baryon peaks the self-gravity of baryons is comparable to the gravitational field due to the collisionless component and this can have an important effect on the evolution of the latter. In general, many peaks in the DM component are associated to a single peak in the BM. These are usually embedded in the corresponding baryonic peak which stays more spread in space because of the effect of pressure working against the collapse. For the highest BM peaks present in the case  $n = -1$  the situation is reversed: the pressure, although higher than in the previous cases, is not able to oppose sensibly the infall of BM and we end up with a distribution in the DM which is more spread than that in the BM. This behaviour is confirmed by the value of the bias which, for  $n = -1$  is larger than one at all scales.

Our analysis is completely scale-free and the final distribution of the gas temperature depends only on the assumed power spectrum. The highest values of the temperature are obtained for the case  $n = -1$  and they correspond to the high density regions. As the spectral index increases, large-scale motion is reduced and this decreases the height of the baryonic peaks and therefore also the final heating of the gas is smaller. Dissipative processes present in the collisional component allow the transformation of kinetic into internal energy and this makes possible the formation of narrow baryonic peaks even in the absence of cooling processes not included in the present work. In our simulations pressure forces have never been able to equal gravitational forces and so the motion of infall is expected to continue even in presence of high temperatures. The inclusion of cooling terms would amplify this effect and possibly cause a fragmentation of baryonic peaks. Work is presently in progress for testing the effect of cooling and heating processes in the evolution of one-dimensional cosmological perturbations. This, however, will require the specification of the physical scales involved in the problem and therefore the scale-free character of the present study will then be lost.

#### ACKNOWLEDGMENTS

We thank Francesco Lucchin and Sabino Matarrese for discussions. This work was partially supported by Italian MURST.

#### REFERENCES

Anninos P., Norman M.L., Clarke D.A., 1994, ApJ, 436, 11  
 Bond J.R., Centrella J., Szalay A.S., Wilson J.R., 1984, ApJ, 210, 515  
 Boris J.P., Book D.L., 1973, J. Comput. Phys. 11, 38  
 Bryan G.L., Norman M.L., Stone J.M., Cen R.Y., Ostriker J.P., 1994, Comput. Phys. Comm., submitted  
 Cen R., 1992, ApJS, 78, 341  
 Cen R.Y., Ostriker J.P., 1992, ApJ, 393, 22

Chiang W., Ryu D., Vishniac E.T., 1989, ApJ, 339, 603  
 Coles P., Melott A.L., Shandarin S.F., 1993, MNRAS, 260, 765  
 Evrard A.E., 1990, ApJ, 363, 349  
 Hernquist L., Katz N.S., 1989, ApJS, 64, 715  
 Hockney R.W., Eastwood J.W., 1981, Computer Simulations Using Particles. McGraw-Hill, New York, NY  
 Kang H., Ostriker J.P., Cen R., Ryu D., Hernquist L., Evrard A.E., Bryan G.L., Norman M.L., 1994, ApJ, 430, 83  
 Katz N., Gunn J.E., 1991, ApJ, 377, 365  
 Quilis V., Ibáñez J.M., Saez D., 1994, A&A, 286, 1  
 Ryu D., Ostriker J.P., Kang H., Cen R., 1993, ApJ, 414, 1  
 Shapiro P.R., Struck-Marcell C., 1985, ApJ, 57, 205  
 Thoul A.A., Weinberg D.H., 1994, preprint, astro-ph/9410009  
 Williams B.G., Heavens A.F., Peacock J.A., Shandarin S.F., 1991, MNRAS, 250, 458  
 Woodward P., Colella P., 1984, J. Comput. Phys., 54, 115  
 Zalesak S.T., 1979, J. Comput. Phys. 31, 335  
 Zel'dovich Ya. B., 1970, A&A, 5, 84

## FIGURE CAPTIONS

**Figure 1.** Sinusoidal test for the single dark matter component: distribution of density fluctuations just before shell crossing. Comparison between the results obtained from N-body (solid line) and Zel'dovich approximation (open squares), when two different numbers of grid-points  $N_g$  are adopted:  $N_g = 2^{10}$  (left) and  $N_g = 2^{15}$  (right).

**Figure 2.** Sinusoidal test for the coupled evolution of baryonic and dark matter components: distribution of density fluctuations after shell crossing. The dotted and solid lines refer to the baryonic and dark matter components, respectively.

**Figure 3a.** The density fluctuation distribution at  $a = 0.5$  for the three different models:  $n = -1$  (top panel),  $n = 1$  (central panel) and  $n = 3$  (bottom panel). The dotted and solid lines refer to the baryonic and dark matter components, respectively. Only about a tenth of the whole grid is displayed.

**Figure 3b.** As Figure 3a, but at the final time  $a = 1$ .

**Figure 4.** The cross-correlation coefficient  $S$  as a function of the Gaussian filtering radius  $R$  (in units of the whole grid  $L$ ) at the time  $a = 0.5$  (dotted line) and  $a = 1$  (solid line) for the different models:  $n = -1$  (left),  $n = 1$  (centre) and  $n = 3$  (right). Error bars (displayed for clarity only at  $a = 1$ ) represent the r.m.s. scatter between the different simulations.

**Figure 5.** The number of peaks  $N_{pk}$  in dark (solid line) and baryonic (dotted line) components as a function of their height  $\delta$  when  $a = 0.5$  (left column) and  $a = 1$  (right column) for the different models:  $n = -1$  (top),  $n = 1$  (centre) and  $n = 3$  (down).

**Figure 6.** The distribution of baryonic density fluctuation  $\tilde{\varrho}_{BM}$ , pressure  $\tilde{p}$  and temperature  $T$  for the case  $n = -1$  at  $a = 1$ . The whole grid is displayed. Pressure is in arbitrary units while temperature is in Kelvin degrees.

**Figure 7.** The cumulative volume filling factor (solid line) and mass fraction (dotted line) as a function of the temperature  $T$  at the final time  $a = 1$  for the different models:  $n = -1$  (left),  $n = 1$  (centre) and  $n = 3$  (right).

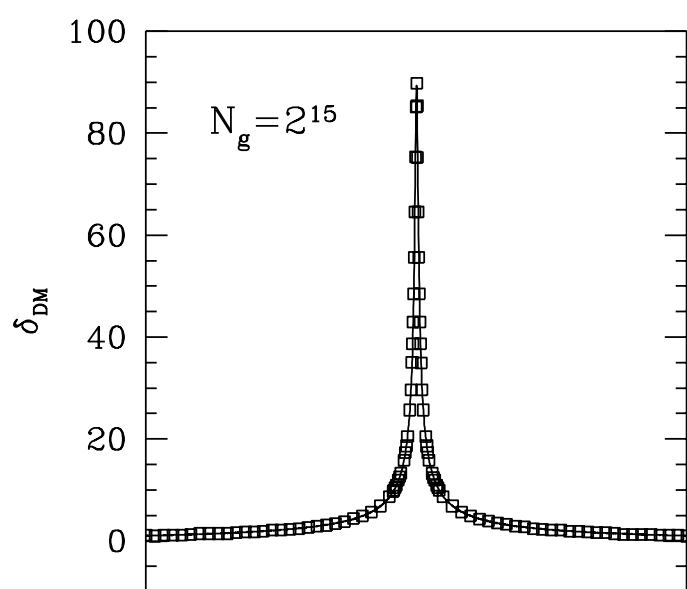
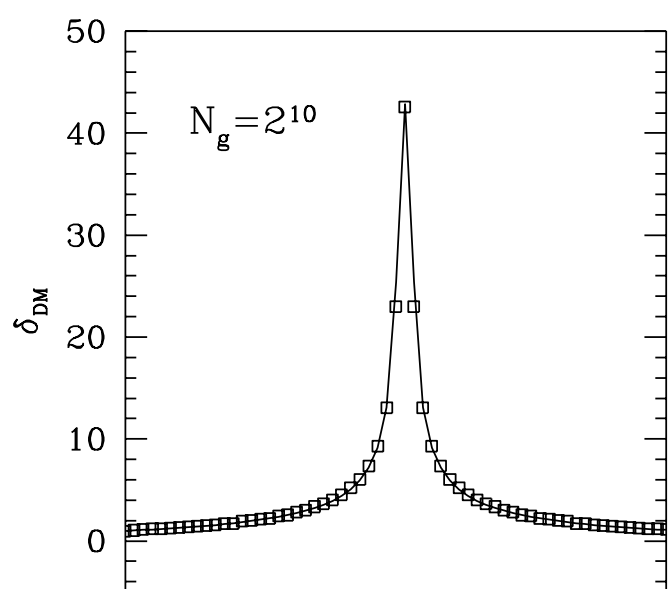
**Figure 8.** Contour plots for the number of grid-points characterized by a given temperature  $T$  and baryonic density  $\tilde{\varrho}$

at the time  $a = 1$  for the different models:  $n = -1$  (left),  $n = 1$  (centre) and  $n = 3$  (right). The contour levels are defined as follows:  $10^{(I/4)}$ , where  $I$  is a positive integer; the outermost contour corresponds to  $I = 4$  and contours inside it have gradually increasing  $I$ .

**Figure 9.** The time evolution of the power-spectrum  $P(k)$  for baryonic (left column) and dark matter (right column) component for the different models:  $n = -1$  (top),  $n = 1$  (centre) and  $n = 3$  (down). The curves refer to different epochs:  $a = 0.09, 0.17, 0.25, 0.33, 0.5$  (dotted lines from down to top) and  $a = 1$  (solid line).

**Figure 10.** The relative bias  $b \equiv \sigma_{BM}/\sigma_{DM}$  as a function of the filtering scale  $R$  at  $a = 0.5$  (dotted line) and  $a = 1$  (solid line) for the different models:  $n = -1$  (left),  $n = 1$  (centre) and  $n = 3$  (right). Error bars (displayed for clarity only at  $a = 1$ ) represent the r.m.s. scatter between the different simulations.

FIGURE 1



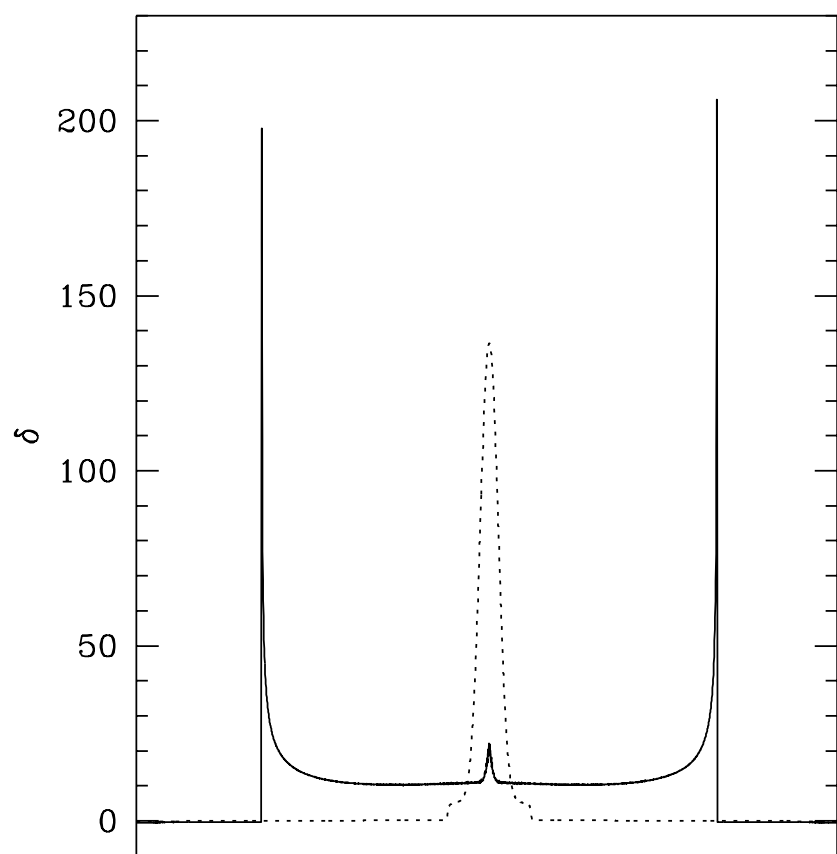
This figure "fig1-1.png" is available in "png" format from:

<http://arxiv.org/ps/astro-ph/9501111v1>

This figure "fig2-1.png" is available in "png" format from:

<http://arxiv.org/ps/astro-ph/9501111v1>

FIGURE 2

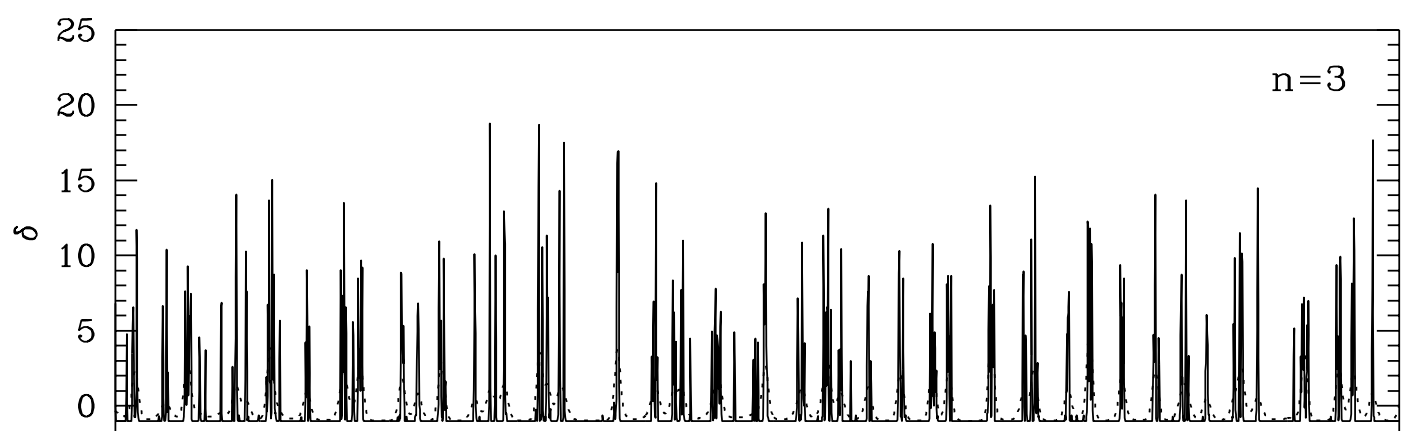
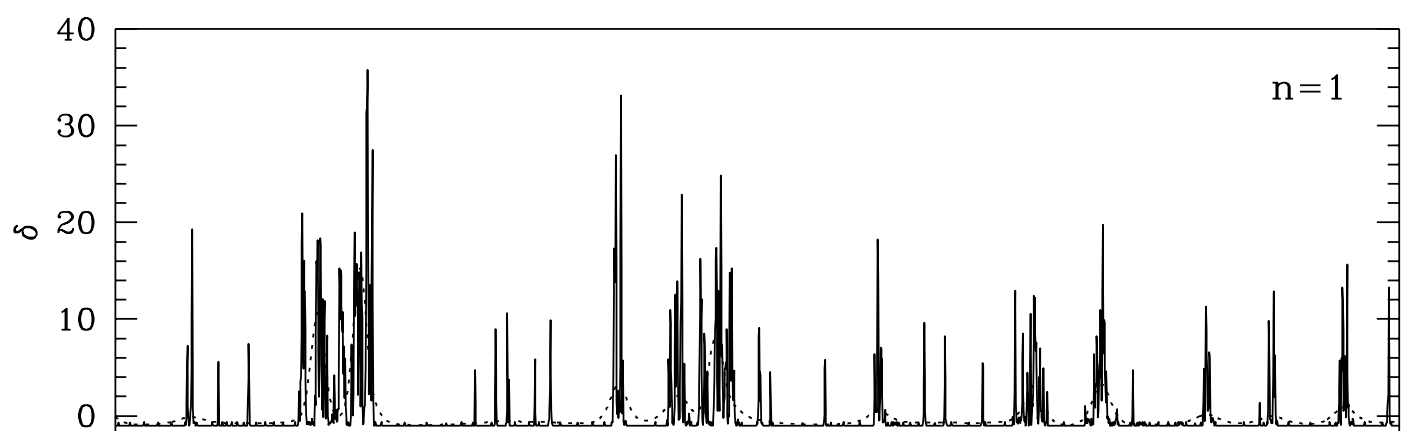
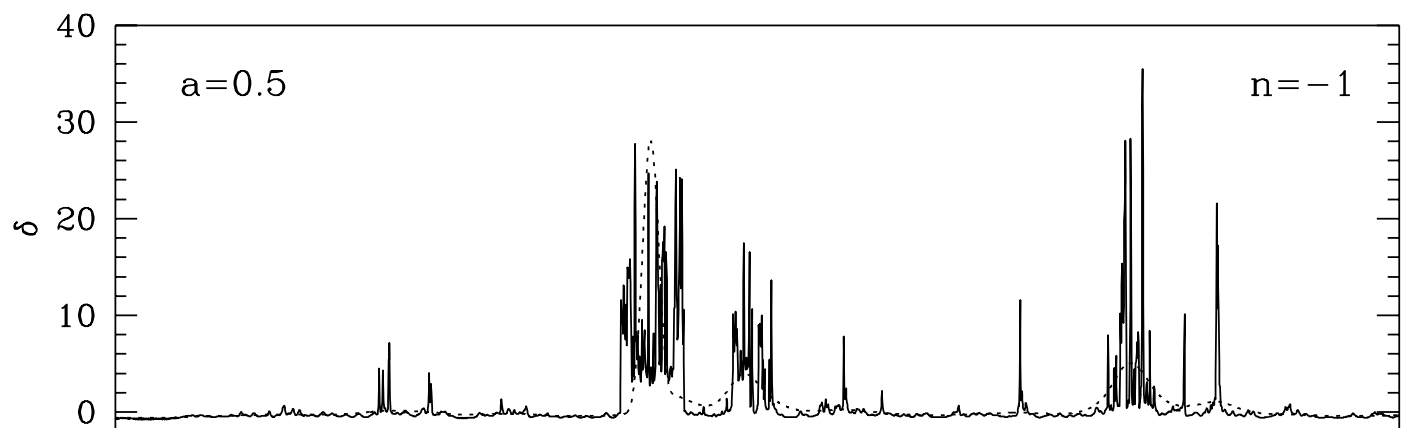


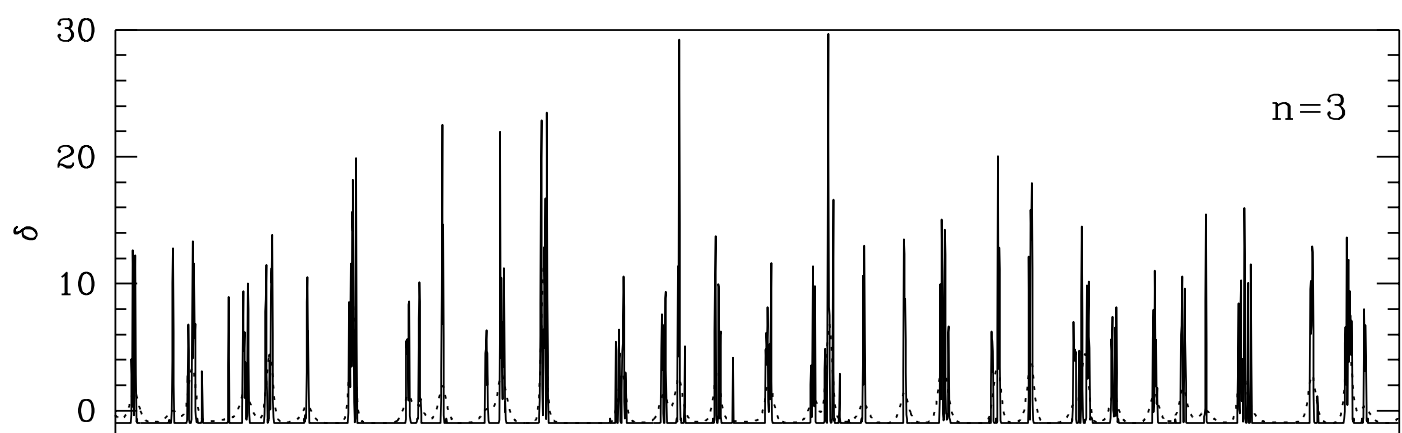
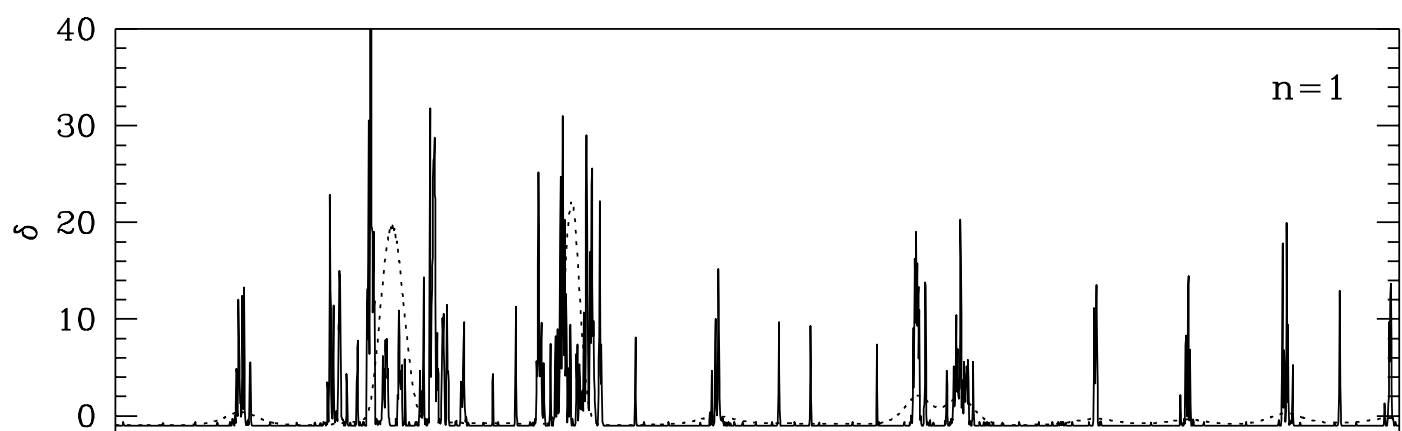
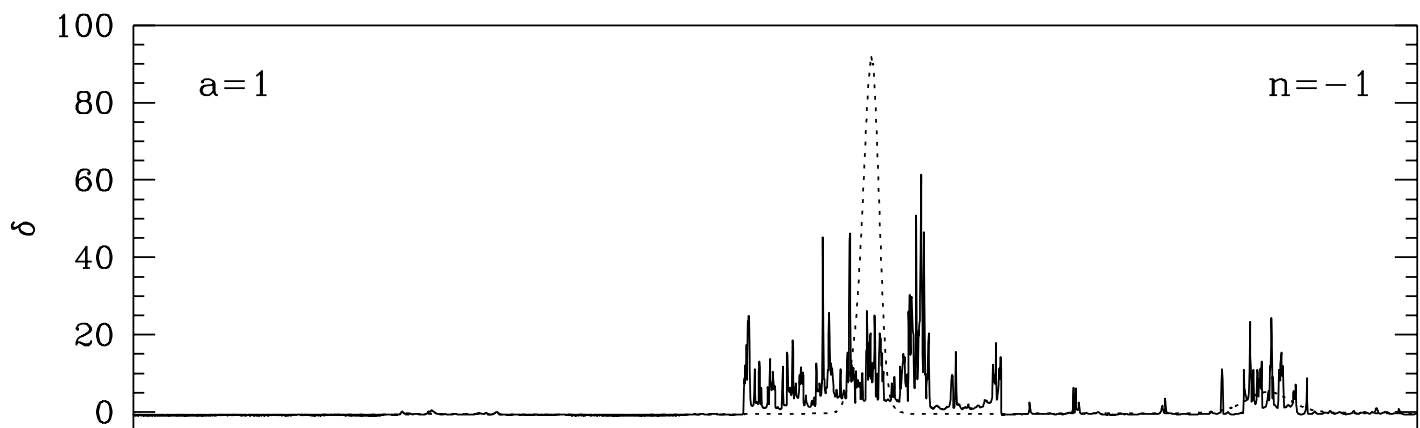
This figure "fig1-2.png" is available in "png" format from:

<http://arxiv.org/ps/astro-ph/9501111v1>

This figure "fig2-2.png" is available in "png" format from:

<http://arxiv.org/ps/astro-ph/9501111v1>





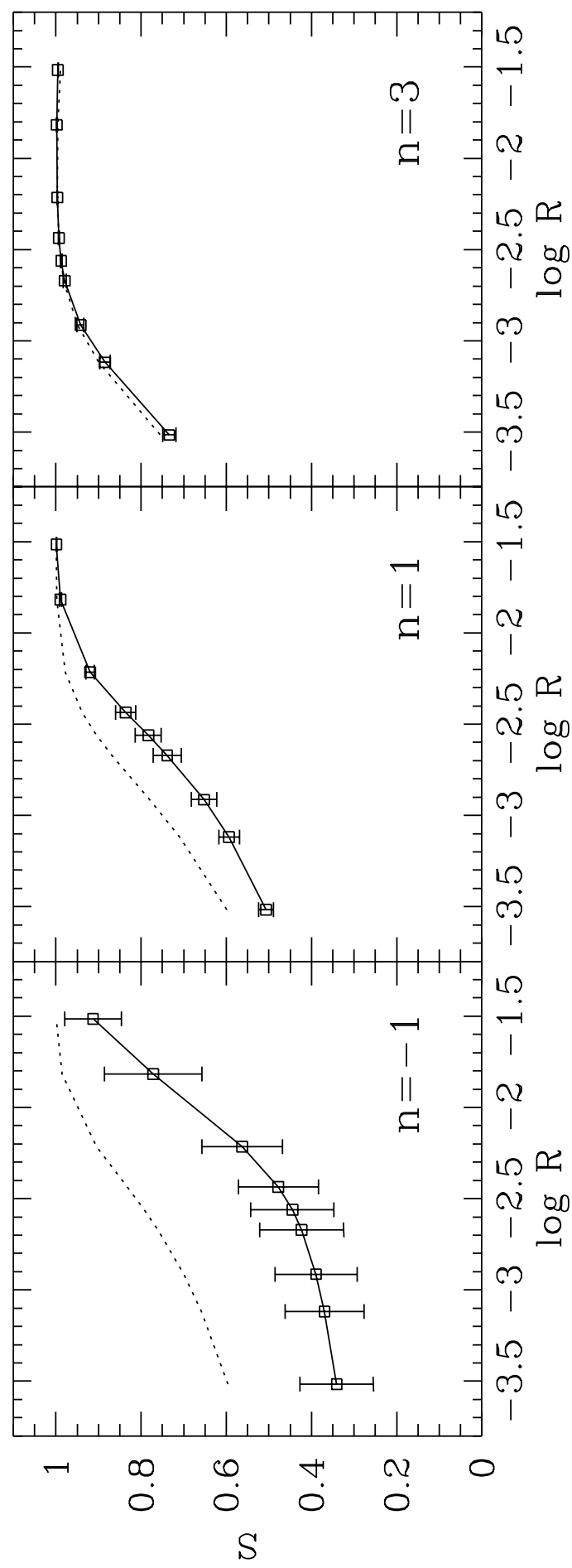
This figure "fig1-3.png" is available in "png" format from:

<http://arxiv.org/ps/astro-ph/9501111v1>

This figure "fig2-3.png" is available in "png" format from:

<http://arxiv.org/ps/astro-ph/9501111v1>

FIGURE 4

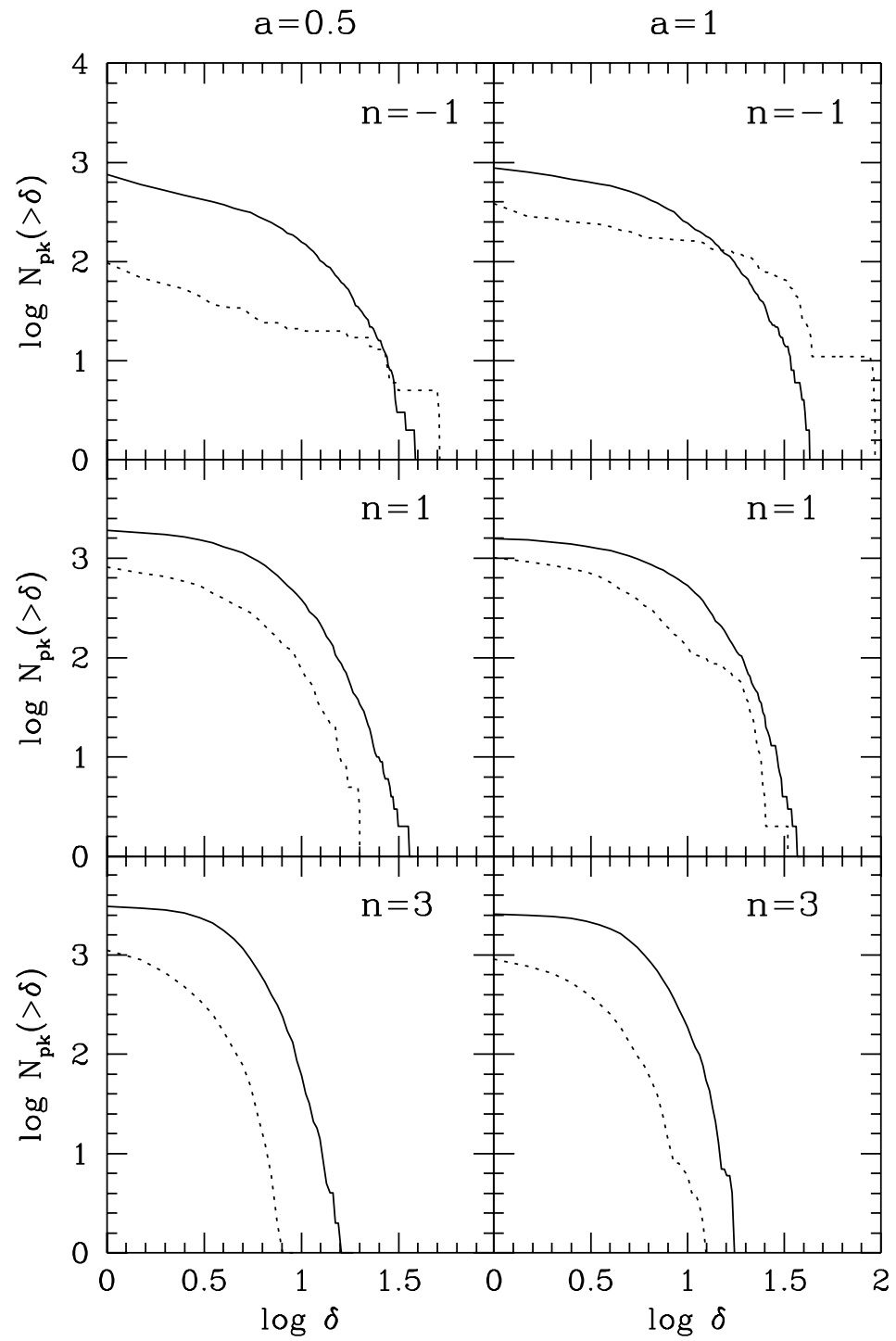


This figure "fig1-4.png" is available in "png" format from:

<http://arxiv.org/ps/astro-ph/9501111v1>

This figure "fig2-4.png" is available in "png" format from:

<http://arxiv.org/ps/astro-ph/9501111v1>

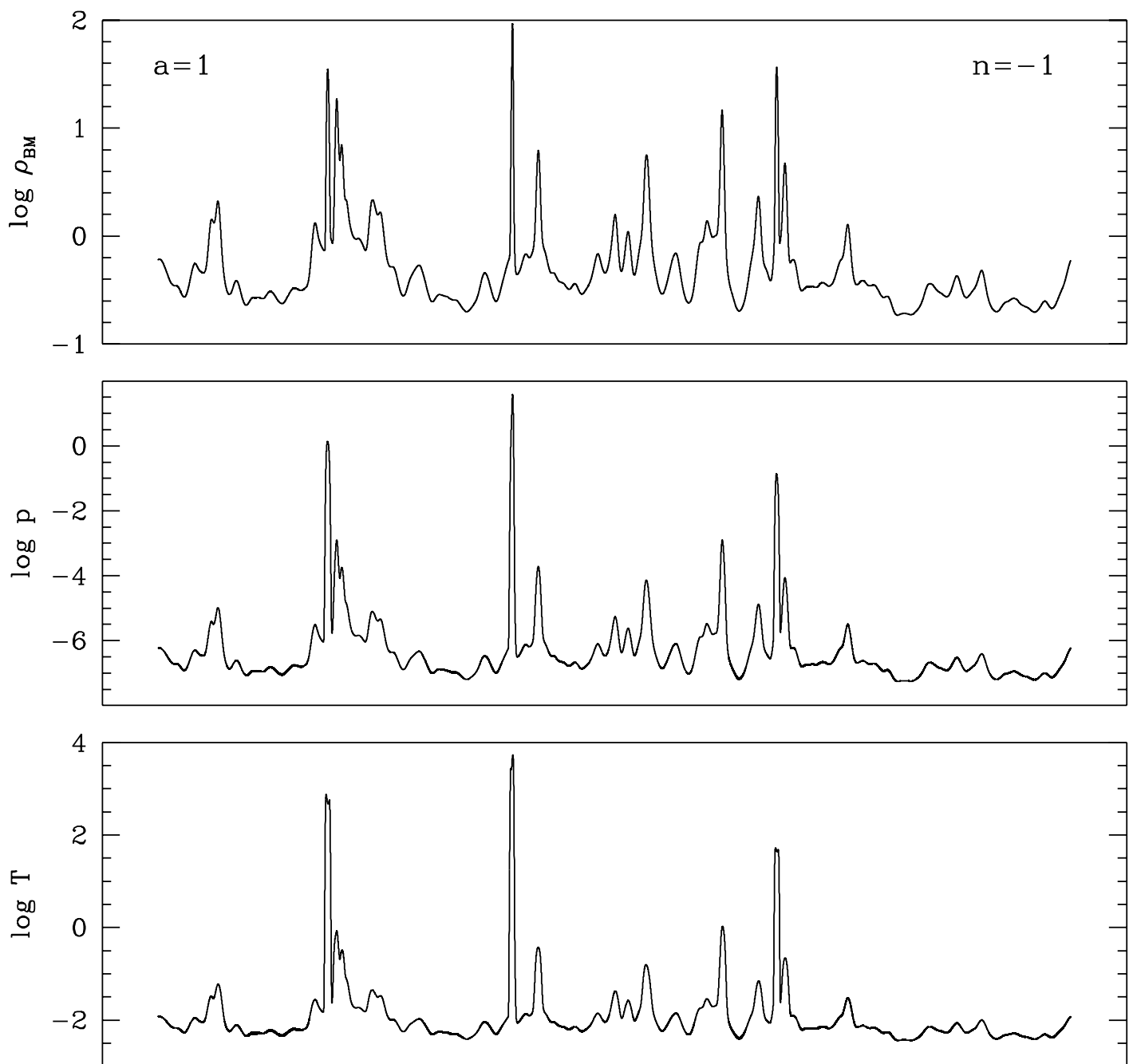


This figure "fig1-5.png" is available in "png" format from:

<http://arxiv.org/ps/astro-ph/9501111v1>

This figure "fig2-5.png" is available in "png" format from:

<http://arxiv.org/ps/astro-ph/9501111v1>



This figure "fig1-6.png" is available in "png" format from:

<http://arxiv.org/ps/astro-ph/9501111v1>

FIGURE  $\gamma$

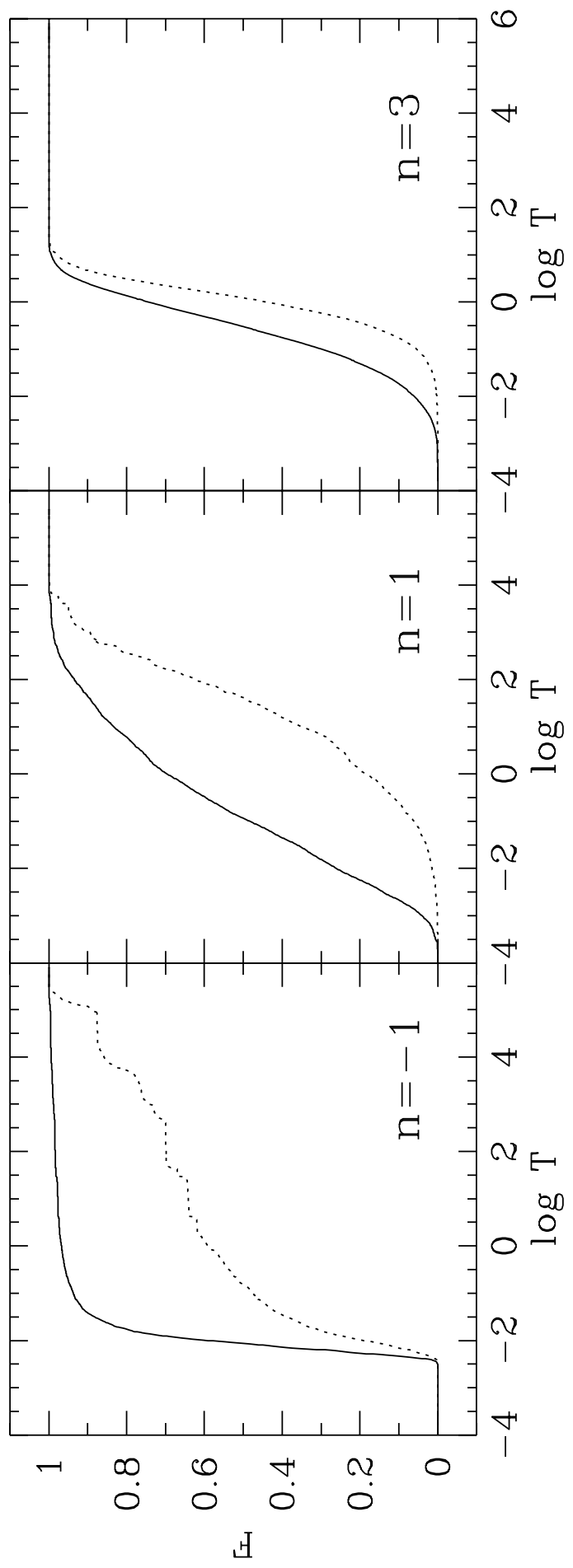
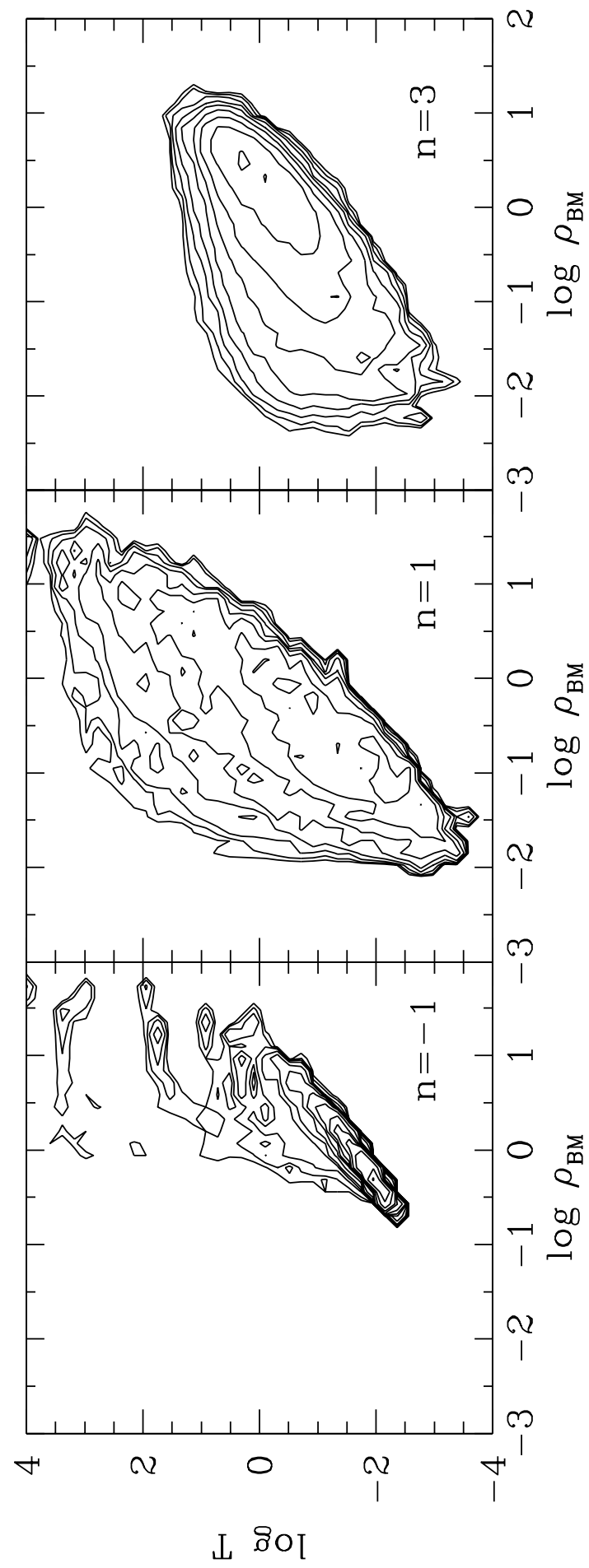


FIGURE 8



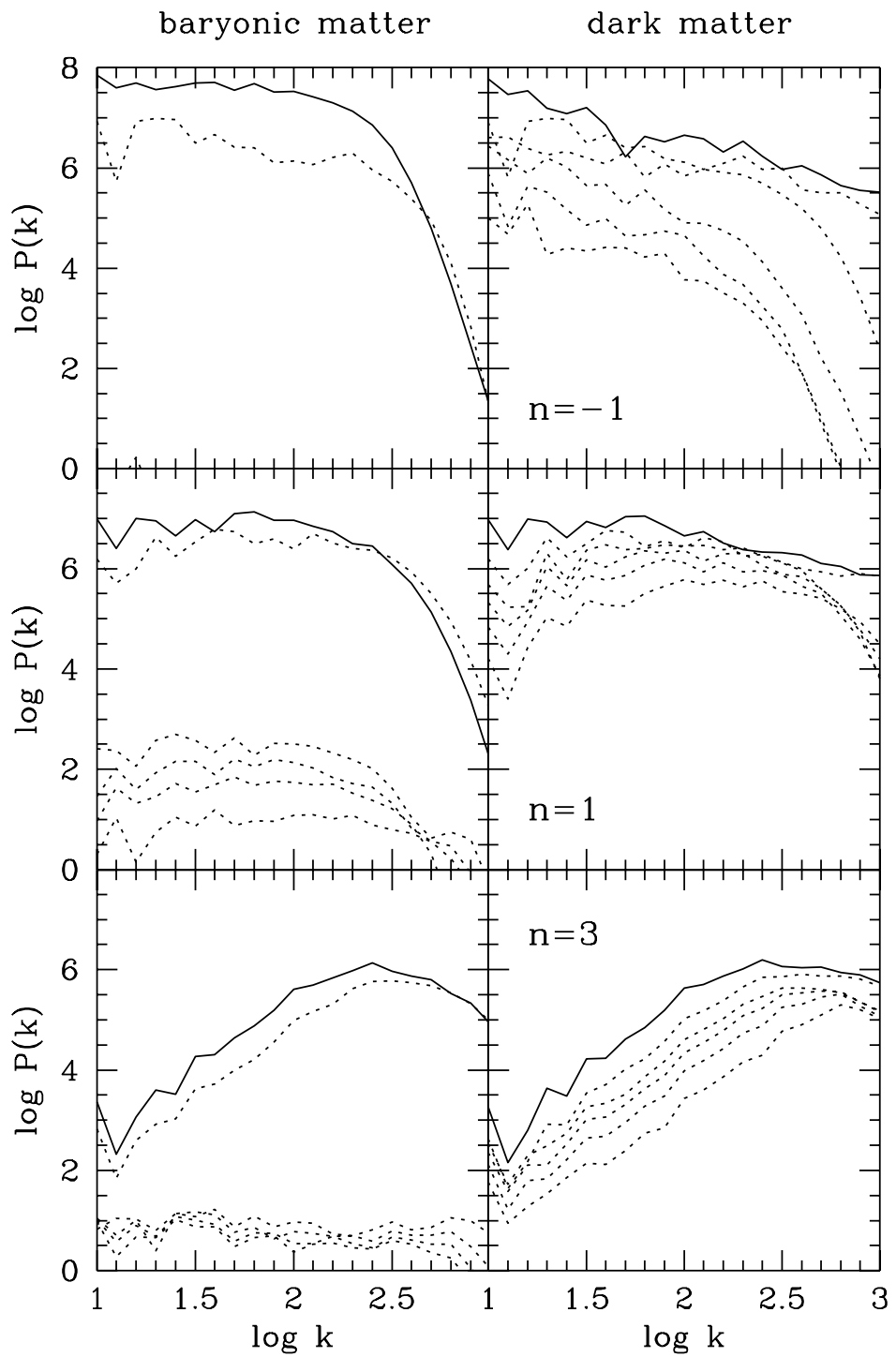


FIGURE 10

